

Plum pudding random medium model of biological tissue toward remote microscopy from spectroscopic light scattering

MIN XU ^{1,*}

¹ Department of Physics, Fairfield University, 1073 North Benson Road, Fairfield, CT 06824, USA

*mxu@fairfield.edu

Abstract: Biological tissue has a complex structure and exhibits rich spectroscopic behavior. There is *no* tissue model up to now able to account for the observed spectroscopy of tissue light scattering and its anisotropy. Here we present, *for the first time*, a plum pudding random medium (PPRM) model for biological tissue which succinctly describes tissue as a superposition of distinctive scattering structures (plum) embedded inside a fractal continuous medium of background refractive index fluctuation (pudding). PPRM faithfully reproduces the wavelength dependence of tissue light scattering and attributes the “anomalous” trend in the anisotropy to the plum and the powerlaw dependence of the reduced scattering coefficient to the fractal scattering pudding. Most importantly, PPRM opens up a novel venue of quantifying the tissue architecture and microscopic structures on average from macroscopic probing of the bulk with scattered light alone without tissue excision. We demonstrate this potential by visualizing the fine microscopic structural alterations in breast tissue (adipose, glandular, fibrocystic, fibroadenoma, and ductal carcinoma) deduced from noncontact spectroscopic measurement.

© 2018 Optical Society of America

OCIS codes: (170.4580) Optical diagnostics for medicine; (170.6510) Spectroscopy, tissue diagnostics; (290.7050) Turbid media; (170.4730) Optical pathology; remote microscopy.

References and links

1. B. Chance, “Optical Methods,” *Ann. Rev. Biophys. Biophys. Chem.* **20**, 1–28 (1991).
2. A. G. Yodh, B. Tromberg, E. Sevick-Muraca, and D. Pine, “Diffusing photons in turbid media,” *JOSA A* **14**, 136–342 (1997).
3. A. M. Laughney, V. Krishnaswamy, E. J. Rizzo, M. C. Schwab, R. J. Barth, D. J. Cuccia, B. J. Tromberg, K. D. Paulsen, B. W. Pogue, and W. A. Wells, “Spectral discrimination of breast pathologies in situ using spatial frequency domain imaging,” *Breast Cancer Res.* **15**, R61 (2013).
4. B. C. Wilson, “Detection and treatment of dysplasia in Barrett’s esophagus: a pivotal challenge in translating biophotonics from bench to bedside,” *J. Biomed. Opt.* **12**, 051401 (2015).
5. W. F. Cheong, S. Prahl, and A. J. Welch, “A review of the optical properties of biological tissues,” *IEEE J. Quant. Electron.* **26**, 2166–2185 (1990).
6. S. L. Jacques, “Optical properties of biological tissues: a review,” *Phys. Med. Biol.* **58**, R37–61 (2013).
7. J. M. Schmitt and G. Kumar, “Optical scattering properties of soft tissue: A discrete particle model,” *Appl. Opt.* **37**, 2788–2797 (1998).
8. M. Xu, T. T. Wu, and J. Y. Qu, “Unified Mie and fractal scattering by cells and experimental study on application in optical characterization of cellular and subcellular structures,” *J. Biomed. Opt.* **13**, 038802 (2008).
9. V. G. Peters, D. R. Wyman, M. S. Patterson, and G. L. Frank, “Optical properties of normal and diseased human breast tissue in the visible and near infrared,” *Phys. Med. Biol.* **35**, 1317–1334 (1990).
10. X. Ma, J. Q. Lu, H. Ding, and X.-H. Hu, “Bulk optical parameters of porcine skin dermis at eight wavelengths from 325 to 1557 nm,” *Opt. Lett.* **30**, 412 (2005).
11. Y. Gazit, D. A. Berk, M. Leunig, L. T. Baxter, and R. K. Jain, “Scale-invariant behavior and vascular network formation in normal and tumor tissue,” *Phys. Rev. Lett.* **75**, 2428–2431 (1995).
12. J. M. Schmitt and G. Kumar, “Turbulent nature of refractive-index variations in biological tissue,” *Opt. Lett.* **21**, 1310–1312 (1996).
13. A. J. Einstein¹, H.-S. Wu, and J. Gil, “Self-affinity and lacunarity of chromatin texture in benign and malignant breast epithelial cell nuclei,” *Phys. Rev. Lett.* **80**, 397–400 (1998).
14. T. Vicsek, *Fluctuation and scaling in biology* (Oxford University Press, New York, 2001).
15. R. K. Wang, “Modeling optical properties of soft tissue by fractal distribution of scatterers,” *J. Mod. Opt.* **47**, 103–120 (2000).

16. M. Xu and R. R. Alfano, "Fractal mechanisms of light scattering in biological tissue and cells," *Opt. Lett.* **30**, 3051–3053 (2005).
17. Y. Pu, W. Wang, M. Al-Rubaiee, S. K. Gayen, and M. Xu, "Determination of optical coefficients and fractal dimensional parameters of cancerous and normal prostate tissues," *Appl. Spectr.* **66**, 828–834 (2012).
18. C. J. R. Sheppard, "Fractal model of light scattering in biological tissue and cells," *Opt. Lett.* **32**, 142–144 (2007).
19. J. D. Rogers, A. J. Radosevich, and V. Backman, "Modeling Light Scattering in Tissue as Continuous Random Media Using a Versatile Refractive Index Correlation Function," *IEEE J. Sel. Top. Quant. Electron.* **20**, 173–186 (2014).
20. X. Wang, B. W. Pogue, S. Jiang, H. Dehghani, X. Song, S. Srinivasan, B. A. Brooksby, K. D. Paulsen, C. Kogel, S. P. Poplack, and W. A. Wells, "Image reconstruction of effective mie scattering parameters of breast tissue in vivo with near-infrared tomography," *J. Biomed. Opt.* **11**, 041106 (2006).
21. M. R. Hajihashemi, S. R. Grobmyer, S. Z. Al-Quran, and H. Jiang, "Noninvasive evaluation of nuclear morphometry in breast lesions using multispectral diffuse optical tomography," *PloS One* **7**, e45714 (2012).
22. M. Xu, M. Alrubaiiee, and R. R. Alfano, "Fractal mechanism of light scattering for tissue optical biopsy," in "Optical Biopsy VI," vol. 6091 of *Proc. SPIE*, R. R. Alfano and A. Katz, eds. p. 60910E, (2006).
23. V. S. Remizovich, "Theoretical description of elastic reflection of particles (photons) incident at grazing angles without the use of the diffusion approximation," *Sov. Phys. JETP* **60**, 290–297 (1984).
24. B. J. Uscinski, H. G. Booker, and M. Marians, "Intensity Fluctuations Due to a Deep Phase Screen with a Power-Law Spectrum," *Proc. Royal Soc. A* **374**, 503–530 (1981).
25. R. Michels, F. Foschum, and A. Kienle, "Optical properties of fat emulsions," *Opt. Express* **16**, 2304–2314 (2008).
26. T. T. Wu, J. Y. Qu, and M. Xu, "Unified Mie and fractal scattering by biological cells and subcellular structures," *Opt. Lett.* **32**, 2324–2326 (2007).
27. M. Xu, "Superposition rule for light scattering by a composite particle," *Opt. Lett.* **31**, 3223–3225 (2006).
28. M. I. Mishchenko, L. D. Travis, and A. A. Lacis, *Scattering, absorption, and emission of light by small particles* (Cambridge University Press, Cambridge, UK, 2002).
29. W. J. Wiscombe, "Improved Mie scattering algorithms," *Appl. Opt.* **19**, 1505–1509 (1980).
30. The codes for the PPRM model, fitting procedures and the data can be found at <http://www.faculty.fairfield.edu/mxu>.
31. A. N. Bashkatov, E. A. Genina, and V. V. Tuchin, "Optical properties of skin, subcutaneous, and muscle tissues: a review," *J. Innov. Opt. Health Sci.* **04**, 9–38 (2011).
32. P. J. Shaw, "Nucleolus," in *Encyclopedia of Life Sciences*, (John Wiley & Sons, Ltd., 2005).
33. H. A. Foster, D. K. Griffin, and J. M. Bridger, "Interphase chromosome positioning in vitro porcine cells and ex vivo porcine tissues," *BMC Cell Biol.* **13**, 30 (2012).
34. K. P. Nielsen, L. Zhao, J. J. Starnes, K. Starnes, and J. Moan, "The importance of the depth distribution of melanin in skin for DNA protection and other photobiological processes," *J. Photochem. Photobiol., B* **82**, 194–198 (2006).
35. V. G. Peters, D. R. Wyman, M. S. Patterson, and G. L. Frank, "Optical properties of normal and diseased human breast tissues in the visible and near infrared," *Phys. Med. Biol.* **35**, 1317–1334 (1990).
36. M. S. J., A. Malinowski, M. Peter Strokorb, M. Oesting, and K. Strokorb, "Analysis, Simulation and Prediction of Multivariate Random Fields with Package {RandomFields}," *J. Stat. Software* **63**, 1–25 (2015).
37. X. Wang, "Estimation of Scatterer Size and Number Density in Near-Infrared Tomography," Ph.D. thesis, Dartmouth College (2007).
38. V. Nandakumar, L. Kelbauskas, K. F. Hernandez, K. M. Lintecum, P. Senechal, K. J. Bussey, P. C. W. Davies, R. H. Johnson, and D. R. Meldrum, "Isotropic 3D nuclear morphometry of normal, fibrocystic and malignant breast epithelial cells reveals new structural alterations," *PloS One* **7**, e29230 (2012).
39. L. F. Barbisan, J. Russo, and M. L. Mello, "Nuclear and nucleolar image analysis of human breast epithelial cells transformed by benzo[a]pyrene and transfected with the c-Ha-ras oncogene," *Anal. Cellular Path.* **16**, 193–199 (1998).
40. R. Drezek, A. Dunn, and R. Richards-Kortum, "A pulsed finite-difference time-domain (FDTD) method for calculating light scattering from biological cells over broad wavelength ranges," *Opt. Express* **6**, 147–157 (2000).
41. R. S. Brock, X.-H. Hu, D. A. Weidner, J. R. Mourant, and J. Q. Lu, "Effect of detailed cell structure on light scattering distribution: FDTD study of a B-cell with 3D structure constructed from confocal images," *J. Quant. Spectr. Rad. Transfer* **102**, 25–36 (2006).
42. M. S. Starosta and A. K. Dunn, "Three-Dimensional Computation of Focused Beam Propagation through Multiple Biological Cells," *Opt. Express* **17**, 12455 (2009).
43. H. K. Roy, Y. Liu, R. K. Wali, Y. L. Kim, A. K. Kromine, M. J. Goldberg, and V. Backman, "Four-dimensional elastic light-scattering fingerprints as preneoplastic markers in the rat model of colon carcinogenesis," *Gastroenterology* **126**, 1071–1081 (2004).
44. K. Badizadegan, V. Backman, C. W. Boone, C. P. Crum, R. R. Dasari, I. Georgakoudi, K. Keefe, K. Munger, S. M. Shapshay, E. E. Sheetse, and M. S. Feld, "Spectroscopic diagnosis and imaging of invisible pre-cancer," *Faraday Discuss.* **126**, 265–279 (2004).
45. Y. Zhu, T. Fearn, G. Mackenzie, B. Clark, J. M. Dunn, I. J. Bigio, S. G. Bown, and L. B. Lovat, "Elastic scattering spectroscopy for detection of cancer risk in Barrett's esophagus: experimental and clinical validation of error removal by orthogonal subtraction for increasing accuracy," *J. Biomed. Opt.* **14**, 044022 (2010).

46. B. Delahunt, J. C. Cheville, G. Martignoni, P. A. Humphrey, C. Magi-Galluzzi, J. McKenney, L. Egevad, F. Algaba, H. Moch, D. J. Grignon, R. Montironi, and J. R. Srigley, "The International Society of Urological Pathology (ISUP) grading system for renal cell carcinoma and other prognostic parameters," *Am. J. Surg. Path.* **37**, 1490–504 (2013).
 47. M. I. Mishchenko, L. D. Travis, and A. A. Lacis, *Scattering, absorption and emission of light by small particles* (Cambridge University Press, 2002).
 48. H. C. van de Hulst, *Light Scattering by Small Particles* (Dover, New York, 1981).
 49. D. Wales and J. Doye, "Global optimization by basin-hopping and the lowest energy structures of Lennard-Jones clusters containing up to 110 atoms," *J. Phys. Chem. A* **5639**, 5111–5116 (1997).
-

1. Introduction

One central tenet in the application of light in biology and medicine is noninvasive diagnosis of the structure and function of tissue from tissue-light interaction [1]. Scattered light carries important information about the morphology and optical properties of the individual scatterers and can be used to identify structural alterations or heterogeneities in tissue due to disease or physiological variations [2–4]. The scattering and absorption properties of tissue determine light transport (such as penetration, reflection, and transmission) and energy deposition in tissue, key to both diagnostic and therapeutic applications of light. Significant advances have been made during the past decades in characterizing and modeling the optical properties of different types of tissue (see, for example, [5, 6], for recent reviews).

Biological tissue has a complex structure which determines the optical properties of tissue. Microstructures in biological tissue range from organelles $0.2 - 0.5 \mu\text{m}$ or smaller, mitochondria $1 - 4 \mu\text{m}$ in length and $0.3 - 0.7 \mu\text{m}$ in diameter, nuclei $3 - 10 \mu\text{m}$ in diameter, to mammalian cells $10 - 30 \mu\text{m}$ in diameter. The refractive index variation is about $0.04 - 0.10$ for soft tissue with a background refractive index $n \approx 1.35 - 1.37$ [7, 8]. When the wavelength, λ , of the probing light increases, light is less scattered by tissue [5, 6] and the reduced scattering coefficient (μ'_s) decreases. Light is also expected to be more isotropically scattered into all directions as the scatterers appear smaller with respect to the wavelength and the anisotropy factor (g) defined as the mean cosine of the scattering angles of tissue gets smaller. This widely-accepted notion about the wavelength dependence of μ'_s and g is, however, only partially true and the trend of g is contradictory to that found by thorough measurements for various tissue types within visible and near-infrared spectral range [6, 9, 10]. The "anomalous" increase of g with the probing wavelength seems to be the rule rather than the exception for tissue light scattering [6].

Viewed on a microscopic scale, the constituents of tissue have no clear boundaries and merge into a continuum structure. Furthermore, many biological tissues have fractal-like organization and are statistically self-similar [11–14]. Light scattering property of a tissue was hence attributed to the fluctuation of the refractive index distribution in tissue. A fractal model [12, 15–17] and later a Whittle-Matern family of correlation functions [18, 19] have been used successfully to describe such fluctuation in tissue. These models show that μ'_s has a powerlaw dependence on the wavelength ($\mu'_s \propto \lambda^{-b}$ with $b > 0$ being the scattering power) and correctly predict the decrease of tissue scattering with λ [16]. Unfortunately, these models *all* predict the decrease of the anisotropy factor g with λ , disagreeing with experimental observations. The anisotropy factor is one central parameter governing how light randomizes its directionality and migrates with scattering in random media and bearing the direct relation to the morphology and optical properties of the underlying microscopic scattering constituents. The contradiction between experiments and theoretical predictions on g reveals the current lack in the understanding of the nature of tissue light scattering. There is *no* tissue model up to now able to account for the observed spectroscopy of scattering and its anisotropy.

Recently, estimation of the effective scatterer size or nuclear morphology in deep tissue from spectroscopic diffuse light measurements have been reported [20, 21]. This could potentially lead to highly desirable *in vivo* optical histopathology of deep tissue from scattered light alone. An accurate yet succinct picture and model of the complex structure of biological tissue will

be the foundation towards this direction, achieving extremely desirable remote microscopy of biological tissue from bulk spectroscopic light scattering without any tissue excision.

In this article, after first reviewing continuum light scattering models for tissue and identifying their deficiency, we present, *for the first time*, a Plum Pudding Random Medium model (PPRM) for biological tissue. PPRM properly describes the scattering constituents in tissue that tissue is a continuum yet with some prominent structures which are distinctive from the background medium. In this unified view, tissue light scattering is a superposition of both background refractive index fluctuation and distinctive prominent structures. The distinctive prominent structure is responsible for the observed “anomalous” anisotropy trend and provides a potential resolution to the long-lasting puzzle in the spectroscopic properties of tissue. Afterwards, by establishing the explicit link of the macroscopic scattering parameters of tissue to the microstructure, we show PPRM opens up a new venue of quantifying the *microscopic* scattering constituents in tissue from *macroscopic* probing of a bulk from scattered light alone. We demonstrate this potential at the end by visualizing the fine microscopic structural alterations in breast tissue (normal adipose tissue, normal glandular tissue, fibrocystic tissue, fibroadenoma, and ductal carcinoma) from PPRM analysis of noncontact spectroscopic measurement.

2. Theory

2.1. Background refractive index fluctuation

One major source for light scattering by tissue is attributed to the random fluctuation of the background refractive index for biological tissues and cells [16, 22]. Denote $S_{\text{bg}}(\mathbf{q})$ the scattering amplitude due to the random fluctuation of the background refractive index. The squared background scattering amplitude is specified by [8]

$$|S_{\text{bg}}(\mathbf{q})|^2 \begin{cases} \mu^2 & \text{(parallel polarized)} \\ 1 & \text{(perpendicular polarized)} \end{cases} = 2\pi k^6 V \hat{R}(q) \begin{cases} \mu^2 & \text{(parallel polarized)} \\ 1 & \text{(perpendicular polarized)} \end{cases} \quad (1)$$

where $\mathbf{q} = q(\cos \phi, \sin \phi, 0)$ is the wave vector transfer with a magnitude $q = 2k \sin \frac{\theta}{2}$, $k = 2\pi n_0 / \lambda$ is the wave number with n_0 the average refractive index of the background medium and λ the wavelength of the incident beam in vacuum, θ , ϕ are the polar and azimuthal angles of scattering, respectively, $\mu \equiv \cos \theta$, V is the volume, and $\hat{R}(q) = \frac{1}{(2\pi)^3} \int R(r) \exp(i\mathbf{q} \cdot \mathbf{r}) d\mathbf{r}$ is the power spectrum of the random fluctuation of the background refractive index specified by its correlation function $R(|\mathbf{r}_1 - \mathbf{r}_2|) = \langle \delta m(\mathbf{r}_1) \delta m(\mathbf{r}_2) \rangle$ with $\langle \delta m(\mathbf{r}) \rangle = 0$. The intensity of scattered parallel or perpendicular polarized light is proportional to the corresponding scattering cross section given by $\overline{|S_{\text{bg}}(\mathbf{q})|^2} / k^2$ for light of respective polarization. The scattering cross section for unpolarized light is given by the mean of the two scattering cross sections for light of parallel or perpendicular polarization. The differential scattering cross section for light scattering into the direction (θ, ϕ) from an incident beam linearly polarized along the x axis ($\phi = 0$) is given by

$$\sigma(\theta, \phi) = 2\pi k^4 V \hat{R}(q) (\sin^2 \phi + \mu^2 \cos^2 \phi). \quad (2)$$

The scattering and reduced scattering coefficients of the medium are then expressed as

$$\mu_{s,\text{bg}} = \int \sigma(\theta, \phi) d\Omega = \frac{\pi}{k^2} \int_{-1}^1 |S_{\text{bg}}(q)|^2 (1 + \mu^2) d\mu, \quad (3)$$

$$\mu'_{s,\text{bg}} = \int \sigma(\theta, \phi) (1 - \mu) d\Omega = \frac{\pi}{k^2} \int_{-1}^1 |S_{\text{bg}}(q)|^2 (1 + \mu^2) (1 - \mu) d\mu \quad (4)$$

after setting V in Eq. (1) to be unity.

The fractal random continuous medium model [16] assumes the correlation function of the random fluctuation of the background refractive index to be

$$R(r) = \beta^2 \left(\frac{r}{l_{\max}} \right)^{4-D_f} \Gamma \left[-(4-D_f), \frac{r}{l_{\max}} \right]. \quad (5)$$

Here the distribution of the correlation length l is given by $\eta(l) = \eta_0 l^{3-D_f} / l_{\max}^{4-D_f}$ ($0 \leq l \leq l_{\max}$) normalized to $\int_0^{l_{\max}} \eta(l) dl = 1$, η_0 is a dimensionless constant, $\beta^2 \equiv \langle \delta m(0)^2 \rangle \eta_0$ represents the effective random fluctuation strength where $\langle \delta m(0)^2 \rangle$ is the squared amplitude fluctuation of the refractive index, D_f is the fractal dimension, and Γ is the incomplete Gamma function. For typical soft tissue, $0 < D_f < 7$ and $\sqrt{\langle \delta m(0)^2 \rangle} \sim 0.01$. The value of $\eta_0 = 4 - D_f$ when $D_f < 4$. The cutoff correlation length l_{\max} is the outer scale and 0 is the inner scale in Eq. (5). Strictly, when $D_f \geq 4$, the inner scale is no longer exactly 0 and η_0 depends also on the nonzero inner scale l_{\min} ($\eta_0 = (4 - D_f) / \left[1 - \left(\frac{l_{\min}}{l_{\max}} \right)^{4-D_f} \right]$ for $D_f \neq 4$ and $\eta_0 = 1 / \log \left(\frac{l_{\max}}{l_{\min}} \right)$ for $D_f = 4$). However, in this case Eq. (5) can still be used as light scattering by fluctuations of a correlation length below the inner scale is much smaller and can be ignored. The background squared scattering amplitude is now

$$|S_{\text{bg}}(\mathbf{q})|^2 = \frac{2}{\pi} \frac{\beta^2 V k^3 X^3}{7 - D_f} {}_2F_1 \left(2, \frac{7 - D_f}{2}, \frac{9 - D_f}{2}, -2(1 - \mu)X^2 \right) \quad (6)$$

if $D_f < 7$ where the size parameter $X \equiv k l_{\max}$ and ${}_2F_1$ is the Gauss hypergeometric function. The fractal continuum medium model bears a close connection to a power law size distribution of scatterers. Indeed, using the approximate amplitude scattering matrix [23] for spherical particles, a discrete particle model assuming a particle size distribution of the power law (number density of particles $\propto a^{-D_f}$ where a is the radius) shall yield the same amplitude scattering function (6) as in the fractal continuous medium model. This illustrates the correlation length l in the fractal continuous medium model may be intuitively interpreted as the *radius* of “fictional” scattering centers present within tissue [22]. The number density of the scattering centers of radius l distributes according to a power law l^{-D_f} .

The Whittle-Matern family of correlation function for the fluctuation of the background refractive index takes the form of

$$R(\mathbf{r}) = \langle \delta m(0)^2 \rangle 2^{1-\nu} |\Gamma(\nu)|^{-1} \left(\frac{r}{l} \right)^\nu K_\nu \left(\frac{r}{l} \right) \quad (7)$$

where K_ν is the modified Bessel function of the second kind. The Whittle-Matern correlation function has been used extensively to model turbulence [24] and was later used to model tissue light scattering [12, 18, 19]. The parameter l is the outer scale. When $-3/2 < \nu < 0$, Eq. (7) can still be used (with an implicit *nonzero* inner scale). The Whittle-Matern random medium model gives:

$$|S_{\text{bg}}(\mathbf{q})|^2 = 2 \langle \delta m(0)^2 \rangle \frac{\Gamma(\nu + \frac{3}{2}) V k^3 X^3}{\pi^{1/2} |\Gamma(\nu)|} \left[1 + 2(1 - \mu)X^2 \right]^{-\nu - \frac{3}{2}} \quad (8)$$

when $\nu > -3/2$ where $X \equiv kl$.

Given the background squared scattering amplitude (6) and (8) specified, respectively, in the fractal and Whittle-Matern models, the scattering properties originating from the background refractive fluctuation is simply determined by Eqs. (2-4). Figure 1 shows the trends of various scattering properties: the scattering coefficient μ_s , the reduced scattering coefficient μ'_s , the anisotropy factor $g \equiv 1 - \mu'_s / \mu_s$, and the scattering power b ($\mu'_s \propto \lambda^{-b}$) predicted by the two models. The scattering power is computed over the spectral range from 500nm to 700nm for the center wavelength 600nm.

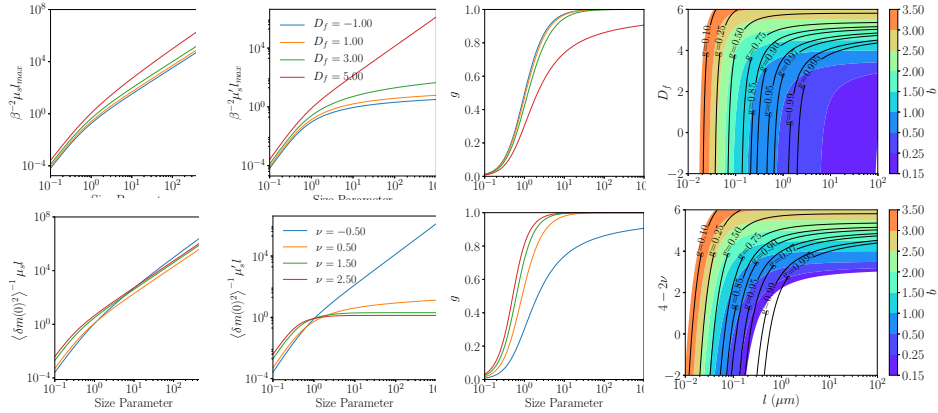


Fig. 1: The normalized scattering coefficient $\beta^{-2}\mu_{s\max} (\langle\delta m(0)^2\rangle^{-1}\mu_s l)$, reduced scattering coefficient $\beta^{-2}\mu'_s l_{\max} (\langle\delta m(0)^2\rangle^{-1}\mu'_s l)$, the anisotropy factor g , and the scattering power b in the fractal (top row) and Whittle-Matern (bottom row) continuous medium model. The size parameter is kl_{\max} and kl , respectively, in the two models. The scattering power b is fitted from $\mu'_s(\lambda)$ over the spectral window $500\text{nm} < \lambda < 700\text{nm}$ centered at 600nm .

For all size parameters, the normalized μ_s , μ'_s , and g in both fractal and Whittle-Matern models increase with the size parameter, i.e., μ_s , μ'_s , and g all decrease with the wavelength. The dependence of their scattering properties on the wavelength reduces to an identical power law if interchanging D_f and $(4 - 2\nu)$ when $X \gg 1$ (see Appendix 4). There are, however, notable differences that first the dependence of the normalized μ_s and μ'_s on D_f in the fractal model is monotonic across the whole size parameters (increases with D_f) whereas it is not the case for the dependence on ν in the Whittle-Matern model. Moreover, the scattering power b is more restrictive in the fractal model than that in the Whittle-Matern model. For example, b stays above 0.25 in the fractal model for a medium of $g = 0.99$ whereas b can be much smaller than 0.25 in the Whittle-Matern model for the medium of an identical anisotropy factor.

Tissue phantoms which consist of only small particles exhibit similar trends [25] as above. Thorough measurements on various tissue types within visible and near-infrared spectral range [9, 10] have revealed unexpectedly contradictory trends in, in particular, g , to the above theoretical prediction as well observed by Jacques in his recent review of optical properties of biological tissues [6]. A pure continuum light scattering model has also been found to be insufficient in an extensive study of angular light scattering of water suspensions of human cervical squamous carcinoma epithelial (HiLa) cells over a wide range of wavelengths (400 to 700nm) [8, 26].

2.2. Plum pudding random medium

The deficiencies of the fractal and Whittle-Matern continuous medium models for tissue light scattering demand a reexamination of the nature of tissue light scattering. Although the refractive index distribution in tissue resembles turbulence yet it is *not* a turbulence. Some prominent structures such as the cell nuclear structure of much higher refractive index than the background are distinctive from the surrounding environment. A more realistic picture of tissue is a composite medium that is a continuum (pudding) yet with some prominent distinctive structures (plum) embedded inside. The superposition principle of light scattering by composite particles [27] provides a convenient framework for describing light scattering by such a system.

Light scattering by Plum Pudding Random Medium model of tissue consists of scattering by distinctive scattering structures and the fluctuation of the background refractive index. The former includes, for example, the nuclear structure in soft tissue and fiber bundles in muscle. The latter incorporates smaller scattering structures such as organelles and refractive index

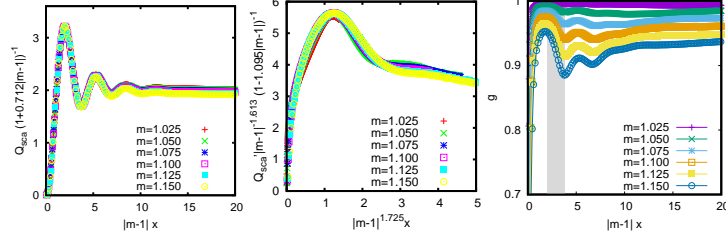


Fig. 2: The scattering efficiencies collapse approximately to one universal curve for $|m - 1| \leq 0.15$ and $0 < x < 200$ after proper scaling. The variations in the anisotropy factor increases with the refractive index m . The shaded region in g within $2 \leq |m - 1|^{-1} x \leq 3.8$ corresponds to the “anomalous” increasing anisotropy factor with the wavelength within the visible and near-infrared spectral range observed in most biological tissues.

variations throughout the tissue continuum. The total squared scattering amplitude, according to the superposition principle of light scattering by composite particles [8, 27], can be written as:

$$\overline{|S(\mathbf{q})|^2} = |S_{\text{core}}(\mathbf{q})|^2 + |S_{\text{bg}}(\mathbf{q})|^2 \quad (9)$$

where $S_{\text{core}}(\mathbf{q})$ represents the scattering amplitude function of the prominent distinctive scattering “cores” and $S_{\text{bg}}(\mathbf{q})$ represents the random fluctuation of the background refractive index described, for example, by the fractal random medium model (6) or the Whittle-Matern model (8).

Now consider light scattering by the prominent distinctive cores in tissue. The cores are of arbitrary shapes and randomly oriented in tissue. The core could be assumed to have a spherical shape after averaging over all these individual ones. Further, the cores can be regarded as optically soft ($|m - 1| \ll 1$ where $m \equiv n_{\text{core}}/n_{\text{bg}}$ is the relative refractive index of the core). To account for the polydispersity of the cores, the radius of the core is assumed to follow a lognormal distribution $f(a)$ on the radius a (see Appendix 4). A different form of particle size distribution may be used. Scatterers of different size distributions but of the same effective radius and effective variance behave alike in their properties of light scattering [28]. The scattering efficiencies for soft particles following the lognormal size distribution of parameters \bar{a} and δ are given by:

$$\bar{Q}_{\text{sca}}(\bar{x}, m, \delta) = \bar{a}^{-2} \int a^2 Q_{\text{sca}}(ka, m) f(a) da, \quad (10)$$

$$\bar{Q}'_{\text{sca}}(\bar{x}, m, \delta) = \bar{a}^{-2} \int a^2 Q'_{\text{sca}}(ka, m) f(a) da \quad (11)$$

respectively where $\bar{x} \equiv k\bar{a}$. Mie theory [29] can be used to compute these efficiencies in general and empirical expressions are given in Appendix 4. The corresponding scattering cross section is given by $\pi\bar{a}^2\bar{Q}_{\text{sca}}$ etc.

The polydispersity of the cores tends to smooth and remove the Mie ripples in the spectral dependence of their scattering properties. To gain insight into the scattering characteristics of such polydisperse soft particles, one representative case of the effective size variance $\nu^{\text{eff}} = 1.0\%$ ($\delta = 0.1$) is shown in Fig. 2. The scattering efficiencies collapse approximately to one universal curve respectively after proper scaling. From this similarity, empirical expressions have been obtained (see Appendix 4). It is clear that the wavelength dependence of the scattering coefficients and the anisotropy factor for such soft particles are not monotonic. There exists multiple regions where their values decrease with the size parameter and increase with the wavelength. In particular, the efficiencies \bar{Q}_{sca} and \bar{Q}'_{sca} reach their maximal values at a size parameter of $2|m - 1|^{-1}$ and $1.245|m - 1|^{-1.725}$, respectively, and the anisotropy factor g decreases with the size parameter (and increases with the wavelength) within $2 \leq |m - 1|^{-1} x \leq 3.8$.

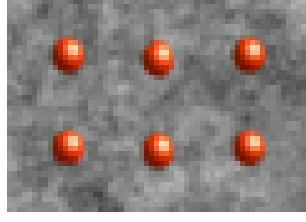


Fig. 3: The Plum Pudding Random Medium model treats tissue as a composite medium with some prominent distinctive structures (plum) embedded inside a continuum (pudding). The former includes, for example, the nuclear structure in soft tissue. The latter incorporates smaller scattering structures such as organelles and refractive index variations throughout the tissue continuum. PPRM faithfully reproduces the wavelength dependence of tissue light scattering and attributes the “anomalous” trend in the anisotropy (g increases with the wavelength) to the plum and the powerlaw dependence of the reduced scattering coefficient on the wavelength to the fractal scattering pudding.

Based on the relationship (9), the bulk scattering properties of the composite medium are then described by the summation from the core (plum) and background fluctuation (pudding) components,

$$\mu_s = \mu_{s,\text{core}} + \mu_{s,\text{bg}} = N_c \pi \bar{a}_c^2 \bar{Q}'_{\text{sca}}(\bar{x}_c, m_c, \delta) + \mu_{s,\text{bg}}, \quad (12)$$

$$\mu'_s = \mu'_{s,\text{core}} + \mu'_{s,\text{bg}} = N_c \pi \bar{a}_c^2 \bar{Q}'_{\text{sca}}(\bar{x}_c, m_c, \delta) + \mu'_{s,\text{bg}} \quad (13)$$

where N_c is the number density of the core with size parameter $\bar{x}_c = k\bar{a}_c$, the refractive index m_c relative to the background, and of a lognormal size distribution with parameter \bar{a}_c and δ , and $\mu_{s,\text{bg}}$ and $\mu'_{s,\text{bg}}$ are given in Eqs. (3, 4).

For most tissues, the size parameter of their core within visible and near-infrared spectral range is less than $1.245 |m_c - 1|^{-1.725}$ and resides in the neighborhood of $2 |m_c - 1|^{-1}$. The anisotropy factor of light scattering, $g = 1 - \bar{Q}'_{\text{sca}}/\bar{Q}_{\text{sca}}$, for the core may increase with the size parameter and decrease with the wavelength (when $\bar{x}_c < 2 |m_c - 1|^{-1}$) or decrease with the size parameter and increase with the wavelength (when $2 |m_c - 1|^{-1} < \bar{x}_c < 3.8 |m_c - 1|^{-1}$). The core in many tissue types belongs to the latter, responsible for the observed “anomalous” anisotropy trend of tissue light scattering (see Fig. 2). Such cores tend to be more dense when the size decreases. The Plum Pudding Random Medium model for tissue is summarized in Fig. 3.

It should be noted that the dependence of the scattering efficiency and the reduced scattering efficiency of the core on the wavelength is mainly through the product of the power of $(m_c - 1)$ and the size parameter, and, in particular, with the former in the form of $(m_c - 1)\bar{x}_c$ and the latter $(m_c - 1)^{1.725}\bar{x}_c$, respectively (see Appendix 4). The simultaneous knowledge of scattering and reduced scattering coefficients can thus decouple $(m_c - 1)$ and \bar{x}_c more reliably than with either parameter alone, enabling accurate determination of both the refractive index and the size of the core.

The determination of the background refractive index fluctuation and the properties of the core completely characterizes and can further depict the microstructure and scattering constituents in biological tissue. That quantification of tissue, although fundamentally from microscopy of a tissue section, offers the quantitative tissue architecture and microscopic structure *on average*. We will term that as *remote microscopy*, derived from non-contact spectroscopic light scattering measurement on a bulk without tissue excision.

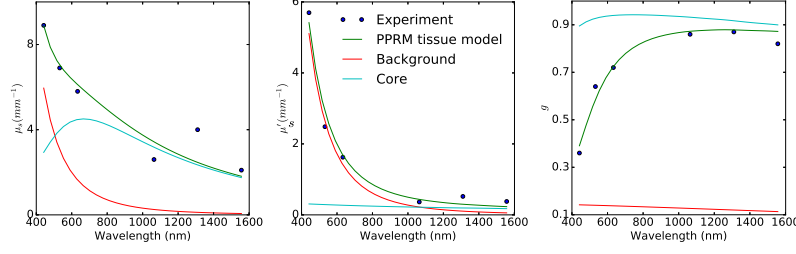


Fig. 4: Plum pudding random medium tissue model fitting of the fresh porcine dermis tissue. The columns from left to right show μ_s , μ'_s and g . The background refractive index fluctuation and the core are shown together with the PPRM tissue model. Experimental data is adapted from Ma et al [10].

3. Results and discussions

Figure 4 shows the PPRM tissue model fitting [30] (see Appendix 4) to the scattering parameters of the fresh porcine dermis tissue measured from diffuse reflectance and transmission using an integrating sphere [10, 31]. Neither the plum nor the pudding alone can fit the data. The parameters from the PPRM fitting is summarized in Table 1. The fitted parameters fully characterizes the tissue and provides microscopic details on the underlying scattering structure. The background refractive index fluctuation has a maximum correlation length $l_{\max} = 0.308\mu\text{m}$ and fractal dimension $D_f = 6.58$. The effective amplitude of the fluctuation is $\beta = 0.545 \times 10^{-3}$, which depends on both the amplitude $\sqrt{\langle \delta m(0)^2 \rangle}$ and the inner scale l_{\min} of the background refractive index fluctuation. The value of β yields $\sqrt{\langle \delta m(0)^2 \rangle} = 0.0115$ assuming the inner scale $l_{\min} = 20\text{nm}$ for the background refractive index fluctuation. This inner scale corresponds to the size of the smallest structure in tissue [7]. The core in the dermis has a concentration of $N_c = 0.473 \times 10^{-3}\mu\text{m}^{-3}$, i.e., one core per cube of size $12.8\mu\text{m}$ on average. The core has an average radius $\bar{a}_c = 0.915\mu\text{m}$ and the relative refractive to the background $m_c = 1.172$. The porcine dermis has a refractive index $n_{\text{bg}} \approx 1.36$ within the spectral range [10] and hence $n_{\text{core}} \approx 1.59$. The core may correspond to the nucleolus which has a substantially higher refractive index than the rest of the nucleus and is of similar size [32, 33]. Another possibility is due to melanosomes whose refractive index ranges between 1.55 – 1.65 [34] as the fresh porcine dermis in the reported experiment contained melanin [10]. The plum (cores) and pudding (background refractive index fluctuation δm) in porcine dermis with parameters specified in Table 1 is shown in Fig. 5.

Table 1: Fitted parameters for fresh porcine dermis tissue. The fluctuation amplitude $\sqrt{\langle \delta m(0)^2 \rangle}$ is computed from β by assuming the inner cutoff for the background refractive index fluctuations to be $l_{\min} = 20\text{nm}$.

Background			Core					
$\beta(\times 10^{-3})$	$l_{\max}(\mu\text{m})$	D_f	$N_c(\mu\text{m}^{-3})$	$\bar{a}_c(\mu\text{m})$	m_c	δ	$\sqrt{\langle \delta m(0)^2 \rangle}$	error
0.545	0.308	6.58	0.473×10^{-3}	0.915	1.172	0.051	0.0115	0.217

The relative importance of the two components (background vs core, or, pudding vs plum) in their contributions to μ_s and μ'_s vary significantly with wavelength. For example, the core contributes 35% to μ_s and the background contributes 94% to μ'_s at 450nm whereas the core contributes 96% to μ_s and the background contributes 30% to μ'_s at 1400nm .

We have also attempted to use the Whittle-Matern model for the background refractive index

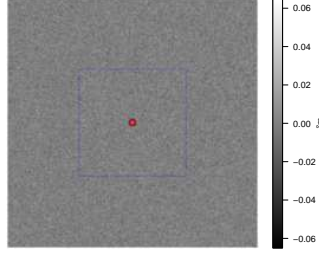


Fig. 5: The plum (core) and pudding (background refractive index fluctuation) in fresh porcine dermis. The whole window size is $30\mu\text{m} \times 30\mu\text{m}$. The blue square delineates a unit cell which contains exactly one core. A core of most probable radius $\bar{a}_c \exp(-\delta^2)$ is shown, surrounded by a shaded area of radius $\bar{a}_c \exp(-\delta^2 + \sqrt{2} \log 2\delta)$ at which the number density of the core drops to half maximum. The core has a relative refractive index $m_c = 1.172$ (“red” color).

fluctuation in the PPRM tissue model to fit the experimental data and were unable to get a satisfactory fitting result. This suggests although both the fractal and Whittle-Matern model have similar behavior at the large size parameter limit they behave quite differently at the low and median size parameter regime and that the fractal model may describe the tissue background refractive index fluctuation more accurately. We hence report only the performance of the PPRM model with the fractal continuum model hereafter.

Most importantly, the Plum Pudding Random Medium tissue model provides a unified platform to characterize the fine details of structure in tissue. The microscopic structural alterations in breast tissue associated with carcinogeneses can be quantified from spectroscopic measurement alone. Figure 6 shows the PPRM tissue model fitting to various disease states of freshly excised and homogenized breast tissue: normal breast adipose tissue, normal glandular breast tissue, fibrocystic tissue, fibroadenoma, and ductal carcinoma reported in [35]. Fibrocystic tissue and fibroadenoma are the most common benign breast conditions. Their fitted parameters are summarized in Table 2. The plum (cores) and pudding (background refractive index fluctuation δm) over a whole window of size $30\mu\text{m} \times 30\mu\text{m}$ for all five types of breast tissue simulated with RandomFields [36] is shown in Fig. 7. The blue square delineates a unit cell which contains exactly one core. A core of most probable radius $\bar{a}_c \exp(-\delta^2)$ is shown, surrounded by a shaded area of radius at which the number density of the core drops to half maximum.

Significant structural alterations can be observed from Table 2 and Fig. 7. The background refractive index of breast tissue is $n_{\text{bg}} \approx 1.36$. The refractive index for the core can be found to be $n_{\text{core}} = 1.49, 1.45, 1.41, 1.44,$ and 1.46 , respectively, for normal breast adipose tissue, normal glandular breast tissue, fibrocystic tissue, fibroadenoma, and ductal carcinoma. The values of n_{core} agree with the respective refractive index of the nucleus in these different breast tissues [20, 21, 37]. The fibrocystic cell nucleus is more round than that in either normal or malignant breast cells and has a radius around $6\mu\text{m}$ [38]. The nucleus of normal and malignant breast cancer cells has more complex structure with the nucleolar size (radius) ranging from $1\mu\text{m}$ to $2\mu\text{m}$ [38, 39]. The core can hence be identified as the nucleus or nucleoli inside a nucleus. The normal adipose tissue is seen to have the background refractive index fluctuation of the smallest fractal dimension ($D_f = 1.56$) and the core with the largest refractive index ($m_c = 1.097$) and biggest size variability ($\delta = 0.177$). The core in the normal fibrocystic tissue has the least concentration ($N_c = 7.76 \times 10^{-5} \mu\text{m}^{-3}$), largest size ($\bar{a}_c = 6.345\mu\text{m}$), smallest refractive index ($m_c = 1.039$) and least size variability ($\delta = 0.004$). The normal glandular breast tissue and fibroadenoma share cores of similar characteristics whereas the background refractive index fluctuation is seen to be with a half fluctuation amplitude ($\beta = 3.34 \times 10^{-3}$ vs 6.93×10^{-3}), a half correlation length ($l_{\text{max}} = 0.111\mu\text{m}$ vs $0.198\mu\text{m}$), and an increase in D_f (5.65 vs 4.59) in the latter than those in the former. Ductal carcinoma is seen to be associated with the core with

the highest concentration ($N_c = 1.83 \times 10^{-3} \mu m^{-3}$) and smallest size ($\bar{a}_c = 1.39 \mu m$).

Similarly, the relative importance of the two components (background vs core, or, pudding vs plum) in their contributions to μ_s and μ'_s vary significantly with wavelength (see Table 3). The core dominates in μ_s whereas the background refractive index fluctuation in μ'_s in general. The importance of the core increases and that of the background decreases with the probing wavelength for both μ_s and μ'_s .

Table 2: Fitted parameters for (a) normal breast adipose tissue, (b) normal glandular breast tissue, (c) fibrocystic tissue, (d) fibroadenoma, and (e) ductal carcinoma. The fluctuation amplitude $\sqrt{\langle \delta m(0)^2 \rangle}$ is computed from β by assuming the inner cutoff for the background refractive index fluctuations to be $l_{\min} = 20\text{nm}$.

	Background			Core			δ	$\sqrt{\langle \delta m(0)^2 \rangle}$	error
	$\beta(\times 10^{-3})$	$l_{\max}(\mu m)$	D_f	$N_c(\mu m^{-3})$	$\bar{a}_c(\mu m)$	m_c			
Adipose	6.08	2.280	1.56	5.46×10^{-4}	2.176	1.097	0.177	0.0039	0.039
Glandular	6.93	0.198	4.59	1.16×10^{-3}	1.820	1.069	0.070	0.0153	0.035
Fibrocystic	5.58	3.524	4.12	7.76×10^{-5}	6.345	1.039	0.004	0.0150	0.020
Fibroadenoma	3.34	0.111	5.65	1.07×10^{-3}	2.054	1.061	0.077	0.0104	0.035
Ductal Carcinoma	3.46	0.561	4.73	1.83×10^{-3}	1.390	1.070	0.066	0.0131	0.034

Table 3: Relative importance of the background refractive index fluctuation (pudding) vs the core (plum) to the scattering coefficient μ_s and the reduced scattering coefficient μ'_s at the probing wavelengths of 500nm and 1100nm.

	μ_s		μ'_s	
	500nm	1100nm	500nm	1100nm
Adipose	46% : 54%	10% : 90%	7% : 93%	6% : 94%
Glandular	12% : 88%	3% : 97%	78% : 22%	49% : 51%
Fibrocystic	80% : 20%	30% : 70%	90% : 10%	81% : 19%
Fibroadenoma	3% : 97%	1% : 99%	66% : 34%	20% : 80%
Ductal Carcinoma	16% : 84%	8% : 92%	75% : 25%	48% : 52%

Biological tissue has a complex structure. The prominent advantage of the Plum Pudding Random Medium model is that it provides a succinct description of the complex structure in terms of a continuous medium of background refractive index fluctuation (pudding) and distinctive prominent structures embedded inside (plum) and faithfully reproduces the observed spectroscopic light scattering properties (μ_s , μ'_s and g) of biological tissue. Both the pudding and the plum are essential for tissue light scattering. The reduced scattering coefficient μ'_s of tissue is dominated by the fractal scattering pudding which yields its powerlaw dependence on the wavelength [16]. Moreover, PPRM provides a potential resolution to the long lasting puzzle that for most biological tissue the anisotropy increases and light scattering is more forward directed with the probing wavelength within visible and near-infrared spectral range. This ‘‘anomalous’’ wavelength dependence of g originates from the core (plum).

PPRM offers a novel analytical platform to understand and interpret light scattering by the complex structures in tissue. In modeling tissue light scattering, PPRM is much more transparent and efficient than the current approaches based on computational expensive FDTD simulations [40–42] which is unable to model real tissue because of its prohibitive computational cost. Most

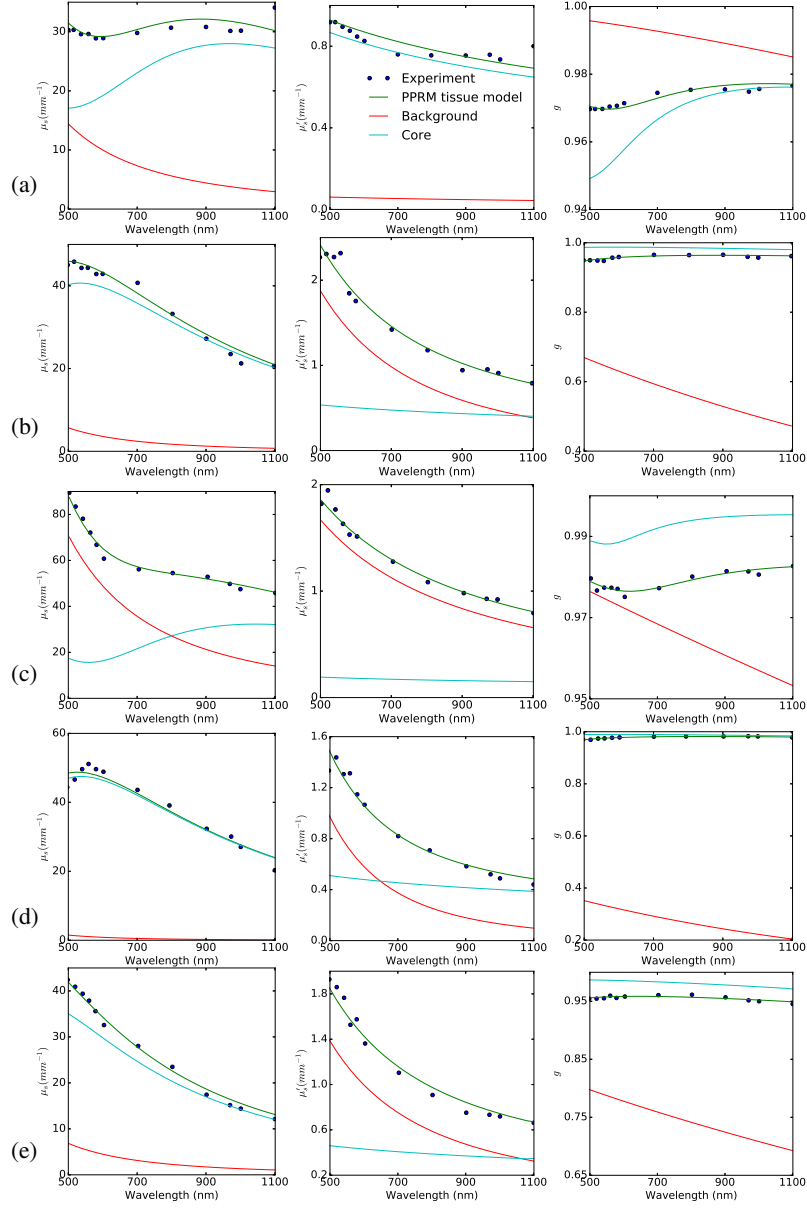


Fig. 6: Plum pudding random medium tissue model fitting to from top row to bottom row (a) normal breast adipose tissue, (b) normal glandular breast tissue, (c) fibrocystic tissue, (d) fibroadenoma, and (e) ductal carcinoma. The columns from left to right show μ_s , μ_s' and g . The background refractive index fluctuation and the core are shown together with the PPRM tissue model. Experimental data is adapted from Peters et al [35].

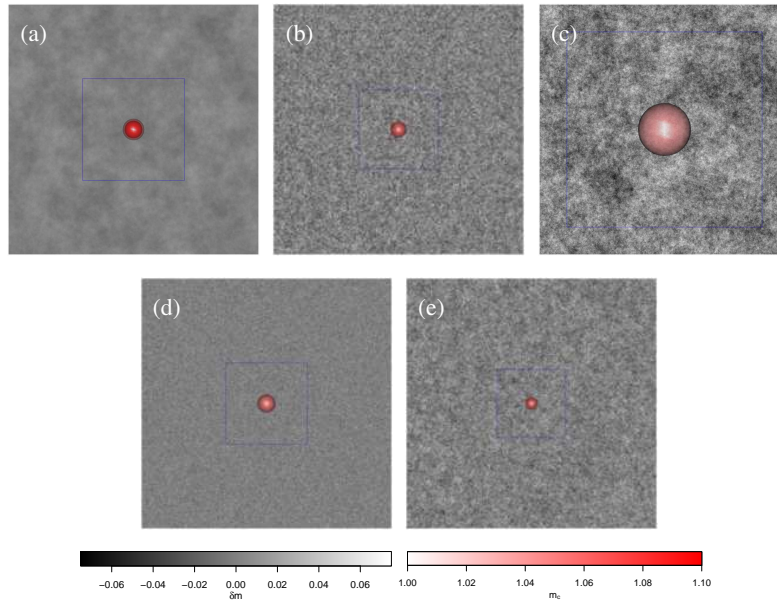


Fig. 7: The plum (core) and pudding (background refractive index fluctuation) in (a) normal breast adipose tissue, (b) normal glandular breast tissue, (c) fibrocystic tissue, (d) fibroadenoma, and (e) ductal carcinoma. The whole window size is $30\mu\text{m} \times 30\mu\text{m}$. The blue square delineates a unit cell which contains exactly one core. A core of most probable radius $\bar{a}_c \exp(-\delta^2)$ is shown, surrounded by a shaded area of radius $\bar{a}_c \exp(-\delta^2 + \sqrt{2 \log 2} \delta)$ at which the number density of the core drops to half maximum.

importantly, PPRM establishes the inherent connection between tissue structure characteristics and its light scattering spectroscopy and opens up a new venue of quantifying the *microscopic* scattering constituents in tissue from *macroscopic* probing of a bulk with scattered light. Fine microscopic structural alterations in tissue associated with cancer or physiological variations can then be deduced from noninvasive macroscopic light scattering spectroscopic measurements. The characteristics of the pudding (background refractive index fluctuation) in tissue has widely been used in early detection and diagnosis of cancer [16, 43–45]. The plum (core) in the PPRM model corresponds to the most prominent scattering structures of higher refractive index in tissue such as the nucleus or the nucleolus. The quantification of such cores is hence of great prognostic value. The smaller nucleolar size has been shown to be correlated with metastatic cells [38]. A new cancer grading system based on the size of the nucleolus has also been recently adopted for renal cell carcinoma, which correlates well with prognosis [46]. The complete tissue characterization by PPRM will hence be instrumental in early detection and diagnosis of tissue diseases including cancer. The deeper understanding of the nature of tissue light scattering also offers important insight in optical sensing strategies that a method interrogating μ_s is preferred to that detecting μ'_s when the core is the target of interest whereas the method detecting μ'_s is better suited for sensing the background refractive index fluctuations and a suitable choice of the probing wavelength can significantly enhance the sensitivity to the target of interest.

4. Conclusions

We have presented here a plum pudding random medium tissue model which captures the key feature of tissue light scattering structures that tissue behaves approximately as a continuum (pudding) yet with some prominent structures (plum) which are distinctive from the background medium. The background refractive index fluctuation is found to be well described by the

fractal continuous medium. The plum pudding random medium model faithfully reproduces the wavelength dependence of tissue light scattering and its anisotropy. It provides a potential resolution to the lasting puzzle that tissue is scattered more into the forward directions by light of longer wavelengths and attributes the “anomalous” trend in the anisotropy of light scattering to the plum whereas the pudding gives rise to the powerlaw dependence of the reduced scattering coefficient on the probing wavelength. Most importantly, the plum pudding random medium model opens up a novel venue of remote sensing of tissue architecture and microscopic structures from spectroscopic light scattering. With a complete quantification of the plum and the pudding of tissue, PPRM accurately depicts fine tissue structural alterations *on average* associated with tissue disease states or physiological variations without excising the tissue.

One prominent advantage of optical methods is the rich spectroscopic content in tissue-light interactions and the potential to probe morphological, biochemical and functional structure of tissue noninvasively. The plum pudding random medium tissue model establishes the quantitative connection between the rich spectroscopic content in light scattering and the underlying tissue microstructure. PPRM may find wide applications in understanding and modeling tissue light scattering, and enabling remote microscopy from spectroscopic scattered light, for example, the promising development in *in vivo* optical histopathology of deep tissue from spectroscopic diffuse light measurement.

Appendix A: The large size limit for the fractal and Whittle-Matern continuum model

See Table 4.

Appendix B: Lognormal size distribution of the core

The radius of the polydisperse core is assumed to follow a lognormal distribution,

$$f(a) = \frac{1}{\sqrt{2\pi}\delta} a^{-1} \exp \left[-\ln^2\left(\frac{a}{\bar{a}}\right)/2\delta^2 \right]. \quad (14)$$

The lognormal size distribution of parameters \bar{a} and δ attains its peak at $\bar{a}/\exp(\delta^2)$ and a full width at half maximum (FWHM) of the size distribution to be $2 \sinh(\sqrt{2 \ln 2} \delta) \bar{a}/\exp(\delta^2)$. The two important characteristics of the size distribution are the effective radius

$$a^{\text{eff}} = \frac{\int_0^\infty a^3 f(a) da}{\int_0^\infty a^2 f(a) da} = \bar{a} \exp(5\delta^2/2) \quad (15)$$

and the effective variance

$$\nu^{\text{eff}} = \frac{\int_0^\infty (a - a^{\text{eff}})^2 a^2 f(a) da}{(a^{\text{eff}})^2 \int_0^\infty a^2 f(a) da} = \exp(\delta^2) - 1. \quad (16)$$

These two characteristics are geometrical projection area weighted. Scatterers of different size distribution but of the same effective radius and variance behave alike in their properties of light scattering [47].

Appendix C: Empirical expressions for light scattering efficiencies of an optically soft particle

The scattering cross section for the core is given by

$$C_{\text{sca}}(x, m) = \pi a^2 Q_{\text{sca}}(x, m) \quad (17)$$

Table 4: The light scattering expressions of the fractal and Whittle-Matern continuous medium model in the limit of $X = kl_{\max}$, $kl \gg 1$ where $\alpha \equiv \langle \delta m(0)^2 \rangle \pi^{1/2} \frac{\Gamma(\nu+3/2)}{|\Gamma(\nu)|}$, and $X = 2\pi n_0 l_{\max} / \lambda$ and $2\pi n_0 l / \lambda$, respectively, in the fractal and Whittle-Matern model. Both models behave alike in this limit and their scattering properties dependence on wavelength reduces to a power law with an identical power if interchanging D_f and $(4 - 2\nu)$.

	Fractal Model	Whittle-Matern Model
μ_s	$\frac{2}{5 - D_f} \beta^2 l_{\max}^{-1} X^2$ $\frac{2^{D_f-5}(23 - 8D_f + D_f^2)}{(D_f - 1)(D_f - 3)} \frac{\pi}{\sin\left(\frac{D_f-5}{2}\pi\right)} \beta^2 l_{\max}^{-1} X^{D_f-3}$	$\frac{4\alpha}{1 + 2\nu} l^{-1} X^2$ $\alpha \frac{(7 + 4\nu^2)}{(3 - 2\nu)(4\nu^2 - 1)} 2^{1-2\nu} l^{-1} X^{1-2\nu}$
	$(D_f < 5)$ $(5 < D_f < 7)$	$(\nu > -\frac{1}{2})$ $(-\frac{1}{2} > \nu > -\frac{3}{2})$
μ'_s	$2 \frac{D_f - 4 + (3 - D_f) \ln(2X)}{(3 - D_f)^2} \beta^2 l_{\max}^{-1}$ $\frac{2^{D_f-3}(D_f^2 - 4D_f + 11)}{(D_f - 3)(D_f^2 - 1)} \frac{\frac{5-D_f}{2}\pi}{\sin\left(\frac{5-D_f}{2}\pi\right)} \beta^2 l_{\max}^{-1} X^{D_f-3}$	$\frac{4\alpha}{4\nu^2 - 1} l^{-1}$ $\alpha \frac{(4\nu^2 - 8\nu + 11)}{(1 - 2\nu)(3 - 2\nu)(5 - 2\nu)} 2^{2-2\nu} l^{-1} X^{1-2\nu}$
	$(D_f < 3)$ $(3 < D_f < 7)$	$(\nu > \frac{1}{2})$ $(\frac{1}{2} > \nu > -\frac{3}{2})$
$1 - g$	$(5 - D_f) \frac{D_f - 4 + (3 - D_f) \ln(2X)}{(3 - D_f)^2} X^{-2}$ $\frac{2^{D_f-5}(D_f^2 - 4D_f + 11)}{(D_f - 3)(D_f^2 - 1)} \frac{(5 - D_f)^2 \pi}{\sin\left(\frac{5-D_f}{2}\pi\right)} X^{D_f-5}$ $2 \frac{(D_f - 5)(D_f^2 - 4D_f + 11)}{(D_f + 1)(23 - 8D_f + D_f^2)}$	$\frac{1}{2\nu - 1} X^{-2}$ $\frac{(1 + 2\nu)(4\nu^2 - 8\nu + 11)}{(1 - 2\nu)(3 - 2\nu)(5 - 2\nu)} 2^{-2\nu} X^{-1-2\nu}$ $-2 \frac{(2\nu + 1)(4\nu^2 - 8\nu + 11)}{(5 - 2\nu)(7 + 4\nu^2)}$
	$(D_f < 3)$ $(3 < D_f < 5)$ $(5 < D_f < 7)$	$(\nu > \frac{1}{2})$ $(\frac{1}{2} > \nu > -\frac{1}{2})$ $(-\frac{1}{2} > \nu > -\frac{3}{2})$

where $x \equiv ka$ is the size parameter with a being the radius of the core and Q_{sca} is the scattering efficiency. In analog to Eq. (17), a similar efficiency can be defined for the reduced scattering cross section C'_{sca} weighted by $1 - \mu$, i.e.,

$$C'_{\text{sca}}(x, m) = \pi a^2 Q'_{\text{sca}}(x, m) \quad (18)$$

The scattering efficiency is very well described by the anomalous diffraction theory for optically soft particles [48]

$$Q_{\text{sca}}(x, m) = 2 - \frac{4}{\eta} \sin \eta + \frac{4}{\eta^2} (1 - \cos \eta), \quad (19)$$

where $\eta \equiv 2x(m - 1)$ is the optical delay for a ray passing through the center of the particle. There are, however, no simple analytical expressions for Q'_{sca} , Q''_{sca} and $\gamma \equiv Q''_{\text{sca}}/Q'_{\text{sca}}$ where Q''_{sca} is defined in a similar fashion to Q'_{sca} with the weighting factor $(1 - \cos \theta)$ replaced by $(1 - P_2(\cos \theta))$ where P_2 is the second order Legendre polynomial. For a size parameter $10 < x < 200$ and $|m - 1| \leq 0.05$, simple empirical expressions can be fitted from the exact Mie solution as following:

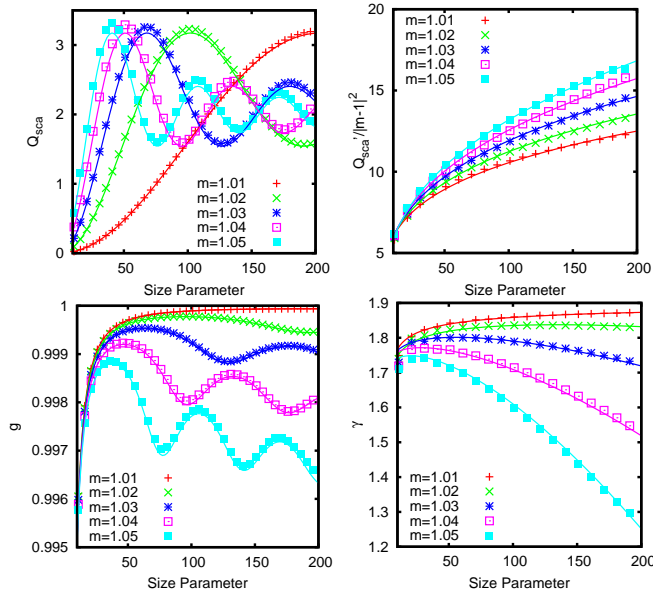


Fig. 8: The scattering efficiency Q_{sca} , the reduced scattering efficiency Q'_{sca} , the anisotropy factor g , and the γ factor for optically soft particle of size parameter $10 < x < 200$. The empirical expressions (in solid lines) and the exact values from Mie theory (in symbols) are shown for $m = 1.01, m = 1.02, \dots, m = 1.05$.

$$Q'_{sca}(x, m) = 2\pi |m-1|^2 (0.578 - 3.256 |m-1|) x^{2.690|m-1|+0.217}, \quad (20)$$

$$Q''_{sca}(x, m) = \gamma(x, m) Q'_{sca}(x, m) \quad (21)$$

and

$$\gamma(x, m) = \frac{32.2 |m-1|^2 - 5.22 |m-1| + 1.929 - (0.1528 |m-1| - 0.00076) \left(\eta - 12.097 + 424.72 |m-1| - 4465.1 |m-1|^2 \right)}{\sqrt{\eta}} \quad (22)$$

The average relative error within the regime is 0.85% and 0.37% for Q'_{sca} and γ , respectively. Their maximum relative error does not exceed 6% and 2%. The anisotropy factor is given by $g(x, m) = 1 - Q'_{sca}/Q_{sca}$. The empirical expressions (in solid lines) and the exact values from Mie theory (in symbols) for Q_{sca} , Q'_{sca} , g and γ are displayed in Fig. 8.

For polydisperse soft particles following a lognormal size distribution, empirical expressions have also been obtained over the region $|m-1| \leq 0.15$ and $0 < x < 200$ for \bar{Q}_{sca} , \bar{Q}'_{sca} and \bar{Q}''_{sca} in the form of $2\pi (1 + d_1 |m-1|) |m-1|^{d_2} \left[c_0 + c_1 - (c_1 + c_3) \frac{\sin(c_4 y)}{c_4 y} \exp(-c_2 y) + 2c_3 \frac{1 - \cos(c_6 y) \exp(-c_5 y)}{(c_6 y)^2} \right]$ where $y \equiv x |m-1|^{d_3}$. The parameters are given in Table 5. The polydispersity of the scatterers averages out the highly oscillatory terms in Mie scattering and hence extends the valid region for the empirical expressions. The value given by the empirical expression for \bar{Q}_{sca} has a mean squared root error of 2.4% and the maximum error less than 5.0% as long as $|m-1| x \geq 1$. When $1 \leq |m-1| x \leq 15$, the value given by the empirical expressions for \bar{Q}'_{sca} has a mean squared root error of 1.8% and the maximum error less than 5.5% whereas the value given by the empirical expression for \bar{Q}''_{sca} has a mean squared root error of 1.5% and the maximum error less than 6.9%. The anisotropy factor g and γ for polydispersed soft particles are plotted in Fig. 9.

Table 5: Parameters for empirical expressions of \bar{Q}_{sca} , \bar{Q}'_{sca} and \bar{Q}''_{sca} .

	c_0	c_1	c_2	c_3	c_4	c_5	c_6	d_1	d_2	d_3
\bar{Q}_{sca}	0	0.3161	0.0768	0.2204	2.0465	-0.0103	1.5213	0.712	0	1
\bar{Q}'_{sca}	0.4292	0.1704	0.3908	1.0386	2.2673	-0.0300	2.6834	-1.095	1.613	1.725
\bar{Q}''_{sca}	0.6572	0.0465	0.6964	1.4930	3.1693	-0.0358	4.0711	-1.642	1.579	1.806

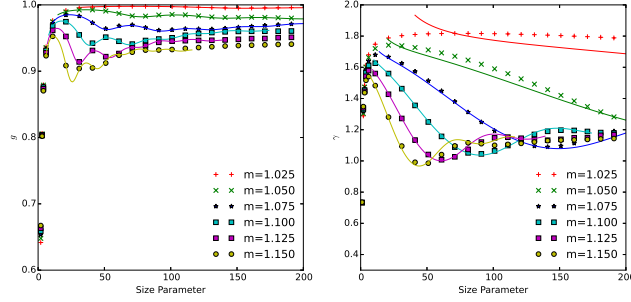


Fig. 9: The anisotropy factor g and γ for polydispersed soft particles ($\nu^{\text{eff}} = 1.0\%$). The symbols are from Mie calculations and the solid lines are from the empirical expressions for $g = 1 - \bar{Q}'_{\text{sca}}/\bar{Q}_{\text{sca}}$ and $\gamma = \bar{Q}''_{\text{sca}}/\bar{Q}'_{\text{sca}}$ over the range $1 \leq |m - 1| x \leq 17.5$.

Appendix D: Fitting procedure

As the reduced scattering is often dominated by the background refractive index fluctuation, we adopt the following multi-step procedure when we fit PPRM to the measured spectroscopic data: (1) Fit the fractal or Whittle-Matern continuum model alone to the observed reduced scattering coefficient data for (l_{max}, D_f) or (l, ν) ; (2) Fit the PPRM tissue model to the observed $g(\lambda)$ for \bar{a}_c , m_c, δ , and N_c by fixing the parameters obtained in (1) unchanged; and (3) Fit the PPRM tissue model to all observed data $\mu'_s(\lambda)$, $\mu_s(\lambda)$ and $g(\lambda)$ using the results from (1) and (2) as the initial guess. To avoid trapping inside a local minimum, global minimization with basin hopping [49] or the particle swarm algorithm is used in the last step.

The fitting error reported in Table 1 and 2 is the mean least squared error defined by

$$\left[\bar{\mu}_{s,\text{meas}}^{-2} \sum_{\lambda} (\mu_{s,\text{mod}} - \mu_{s,\text{meas}})^2 + \bar{\mu}'_{s,\text{meas}}{}^{-2} \sum_{\lambda} (\mu'_{s,\text{mod}} - \mu'_{s,\text{meas}})^2 + \bar{g}_{\text{meas}}{}^{-2} \sum_{\lambda} (g_{\text{mod}} - g_{\text{meas}})^2 \right]^{1/2}$$

between the model (“mod”) and the measurement (“meas”) where $\bar{\mu}_{s,\text{meas}}$ etc are the average of the measured data to homogenize the contributions from μ_s , μ'_s and g .

Funding

NIH (1R15EB009224); DOD (W81XWH-10-1-0526).

Acknowledgements

This work was supported by (1R15EB009224) and DOD (W81XWH-10-1-0526). We thank Swapan K Gayen and Al Katz of City College of New York for their useful comments.

This figure "schematic2b.png" is available in "png" format from:

<http://arxiv.org/ps/1709.00795v1>

This figure "mxuF6a.png" is available in "png" format from:

<http://arxiv.org/ps/1709.00795v1>

This figure "mxuF6b.png" is available in "png" format from:

<http://arxiv.org/ps/1709.00795v1>

This figure "mxuF6c.png" is available in "png" format from:

<http://arxiv.org/ps/1709.00795v1>

This figure "mxuF6d.png" is available in "png" format from:

<http://arxiv.org/ps/1709.00795v1>

This figure "mxuF6e.png" is available in "png" format from:

<http://arxiv.org/ps/1709.00795v1>